machines

MDPI

Article

Estimation-Based Adaptive Online LQI-Stanley Integrated Path Tracking Control for Autonomous Vehicles

Bilal Sevim [1] and Mumin Tolga Emirler [1,2,*]

[1] Department of Control and Automation Engineering, Yildiz Technical University, Istanbul 34220, Türkiye; bilal.sevim@std.yildiz.edu.tr
[2] Department of Aviation Electrics and Electronics, Yildiz Technical University, Istanbul 34220, Türkiye
* Correspondence: emirler@yildiz.edu.tr

Abstract

This study presents an innovative, integrated control architecture combining adaptive online linear quadratic integral (AOLQI) and Stanley geometric control systems for autonomous vehicle path tracking. A key feature of the proposed framework is the offline optimization of the AOLQI parameters using the Particle Swarm Optimization (PSO) algorithm. To address varying road conditions, a Forgetting Factor Recursive Least Squares (FFRLS) algorithm is employed for real-time tire cornering stiffness estimation, complemented by a Kalman–Bucy filter for high-fidelity vehicle side-slip angle observation. The efficacy of this architecture is validated through MATLAB/Simulink and IPG CarMaker co-simulations across demanding benchmarks, including a 100-m radius circular path, the high-speed Hockenheim race track and the high-curvature Stelvio Pass road profile. Numerical evaluations demonstrate that, compared to the conventional LQI, the proposed approach achieves reductions in root mean square error (RMSE) of 44.85%, 24.76% and 51%, and decreases in integral square error (ISE) of 69.2%, 43.16% and 75.86% respectively, in these different scenarios. These results confirm that using an integrated approach with adaptive online LQI and Stanley control, alongside an estimation layer, ensures superior tracking precision and performance improvements across extreme road geometries.

Keywords: path tracking; autonomous vehicle; LQI control; PSO; Stanley control; FFRLS algorithm; Kalman–Bucy filter

1. Introduction

The integration of transportation systems into urban and inter-city environments is an integral part of modern daily life. It is well established that rapid urbanization and population growth correlate with increased traffic density and accident risks. Consequently, autonomous vehicle control has become a focal point of academic and industrial research. Studies in this field encompass critical challenges such as path tracking control, obstacle avoidance, and velocity tracking control.

Vehicle path tracking control can be categorized into two distinct modes: lateral and longitudinal vehicle dynamics control. Lateral control is of indispensable importance for driving stability and operational safety, as maintaining precise control becomes increasingly challenging during high-speed lane changes or aggressive maneuvers. In this study, lateral control strategies for path tracking systems are designed and tested across different simulation scenarios.

Check for updates

Academic Editors: Ossama Mokhiamar and Dan Zhang

Received: 8 July 2026
Revised: 9 September 2026
Accepted: 15 September 2026
Published: 17 September 2026

Copyright: © 2026 by the authors. Licensee MDPI, Basel, Switzerland. This article is an open access article distributed under the terms and conditions of the Creative Commons Attribution (CC BY) license.

In 2015, Emirler et al. developed a robust PID controller for autonomous vehicle path tracking, utilizing high-resolution offline digital maps and real-time GPS data to minimize lateral deviation and yaw angle errors [1]. This tracking framework was subsequently integrated with an elastic band algorithm by Emirler et al. in 2016 to incorporate social safety distances and prevent collisions with vulnerable road users, such as pedestrians and cyclists [2].

In 2018, Wang et al. developed robust PID controller designs based on the parameter space approach, enabling autonomous vehicles to maintain safe path tracking. This framework was integrated with a socially acceptable elastic band algorithm to prevent collisions with pedestrians and was validated through real-world field tests [3]. Subsequently, the PID control design was further enhanced using a multi-objective approach in the discrete-time domain (z-domain) to satisfy simultaneous frequency constraints, such as phase and gain margins. This advanced design was successfully verified through comprehensive autonomous vehicle simulations [4].

In 2019, Emirler designed a Linear Quadratic Integral (LQI) control system featuring speed-dependent gain adaptation to address varying vehicle speeds. The performance of this adaptive control strategy was rigorously evaluated against conventional PID and Linear Quadratic Regulator (LQR) methods under both constant and variable speed profiles. The comparative analysis demonstrated the superior tracking accuracy and robustness of the gain-scheduled LQI approach over the benchmark controllers [5].

In recent years, LQI control frameworks have gained significant traction across a broad spectrum of engineering disciplines. Research by Tajdari et al. (2022) exemplifies this trend, where an LQI-based architecture was developed to optimize traffic capacity at highway bottlenecks by integrating lane-changing maneuvers with ramp-metering strategies for semi-autonomous vehicles [6]. The applicability of LQI controllers, however, extends far beyond autonomous driving; these systems have been increasingly deployed in domains with highly distinct dynamics, such as AC-DC [7], DC-DC power converters [8], energy storage systems [9], aerospace vehicles, and sophisticated robotic manipulators. For instance, the recent literature highlighted the successful application of LQI architectures in flexible robotic arms (2022) [10], helicopter systems (2024) [11], and unmanned aerial vehicles (2025) [12,13], all yielding superior performance metrics. These studies consistently demonstrated that LQI-based designs, when benchmarked against conventional control methodologies, provide substantial enhancements in system tracking accuracy, as evidenced by rigorous quantitative evaluations.

In the field of control systems engineering, the precise calibration of controller parameters is fundamental to ensuring system performance. The existing literature extensively utilizes parameter optimization techniques for synthesizing LQR, PID, and LQR-based hybrid control frameworks. More recently, there has been a significant surge in research focused on elevating the performance of LQI control systems through various heuristic optimization algorithms. A notable example is the work by Sevim and Emirler (2024) [14], who integrated the Particle Swarm Optimization (PSO) algorithm with an LQI controller for autonomous vehicle path tracking, resulting in superior performance metrics. Furthermore, the deployment of optimization meta-heuristics, such as PSO and Genetic Algorithms (GA), within LQI frameworks has proven effective across diverse robotic applications, ranging from fire-suppression robots to unmanned aerial vehicles. These integrated strategies have yielded substantial advancements in both the transient and steady-state responses of complex control architectures [15–17].

The performance of a vehicle control algorithm is fundamentally contingent upon the accuracy of state variable measurements and the fidelity of tire models. The recent literature has established the real-time estimation of vehicle state and tire cornering stiff-

ness as a crucial paradigm for high-precision autonomous driving [18,19]. The proposed approach presents the design of an Adaptive Online LQI (AOLQI) control system that incorporates real-time estimation of critical variables, including the vehicle side-slip angle and tire cornering stiffnesses. By utilizing these estimations, the proposed framework calculates optimal control gains to achieve a fully online LQI architecture. The systematic application of the proposed controller follows a multi-stage optimization process: Initially, the Q and R weighting matrices are optimized using the PSO algorithm to establish baseline controller parameters. Subsequently, a Kalman–Bucy filter and an FFRLS-based estimation layer are integrated to compute instantaneous updates for side-slip angle and cornering stiffnesses. Finally, by incorporating velocity as a time-varying input, a comprehensive Adaptive Online LQI controller is realized, capable of dynamic adaptation to varying vehicle dynamics. Moreover, a geometric control system is added to the proposed architecture to improve performance under high-speed maneuvers and dynamic driving conditions. This framework is synthesized by integrating the Stanley geometric controller into the aforementioned AOLQI architecture. The inclusion of a geometric control component is specifically intended to mitigate path tracking discrepancies during aggressive vehicular maneuvers. The foundation of the Stanley controller dates back to the 2005 DARPA Grand Challenge, where it introduced a paradigm shift by utilizing front-wheel orientation dynamics rather than rear-axle motion. This innovative focus ensures high-fidelity path tracking for high-velocity scenarios [20].

Following the success of the original Stanley algorithm, several advancements have expanded its operational scope. In 2022, the algorithm was merged with B-spline-based geometric path planning to effectively manage complex roundabout geometries and high-curvature trajectories [21]. Concurrently, for electric vehicles featuring four-wheel independent steering, driving, and braking (4WIS/4WID/4WIB), Stanley-based architectures were modernized to incorporate yaw rate tracking, thereby enhancing overall system performance [22].

Recent investigations in 2023 demonstrated that integrating active rear-wheel steering (RWS) with Stanley dynamics significantly enhances lane-keeping performance and system robustness against exogenous disturbances such as crosswinds [23]. Furthermore, to alleviate the adverse effects of sensor and steering actuator latencies, feedforward enhancements considering road curvature were introduced, reducing cross-track errors by 68% without increasing computational overhead [24]. By 2024, the fusion of Stanley with more complex predictive structures led to the development of the model predictive and Stanley (MPS) hybrid controller, which optimizes trajectory tracking for both rectilinear and curved path segments [25]. Similar hybridization strategies, combining Stanley and PID logic, were deployed to correct front-wheel misalignment and rear-distance deviations, providing enhanced tracking precision compared to standalone conventional controllers [26]. Most recently, in 2025, an adaptive double closed-loop path tracking strategy was proposed to achieve high-precision control for agricultural machinery, further pushing the boundaries of Stanley-based control in complex operational environments [27].

Leveraging a conventional LQI framework, this study proposes an online controller design that incorporates instantaneous tire cornering stiffness and vehicle side-slip angle estimation with vehicle velocity measurements. To establish an optimal baseline, a preliminary phase is executed using a Particle Swarm Optimization (PSO) algorithm to fine-tune the LQI weight matrices prior to the online computational process. Ultimately, an Adaptive Online LQI (AOLQI) controller, augmented with a Stanley tracking algorithm, is developed and tested within a MATLAB/Simulink and IPG CarMaker co-simulation environment. The efficacy of the proposed control architecture is benchmarked against a standard LQI framework and a Stanley controller. Furthermore, a comparative performance

analysis is conducted between the proposed integrated system and standalone AOLQI and PSO-optimized AOLQI configurations to validate the enhancements in tracking precision and performance.

To clearly distinguish the proposed architecture from the existing path tracking literature, the core novelties of the AOLQI+PSO+Stanley framework are highlighted across three categories.

First, unlike prior works [1,2,5,14,28,29] that assume constant tire cornering stiffnesses and neglect vehicle side-slip angle estimation, this study introduces an active dual-layer estimator by coupling a Forgetting Factor Recursive Least Squares (FFRLS) cornering stiffness estimator with a Kalman–Bucy filter for vehicle side-slip angle estimation.

Second, rather than using static, pre-computed gain-scheduling tables, the state-space matrices of the system model are reconstructed online. Using these updated matrices, the Algebraic Riccati Equation (ARE) is solved on the fly to continuously compute the optimal control gains. Offline Particle Swarm Optimization (PSO) is executed to establish the optimal baseline weighting matrices (Q, R), eliminating manual tuning.

Third, the proposed approach integrates AOLQI control and geometric error correction provided by Stanley controller. While the AOLQI component guarantees steady-state offset elimination, the superimposed Stanley controller supplies rapid transient steering corrections during severe cornering maneuvers. This hybrid dynamic-geometric approach achieves smooth actuator demand even under low-friction surface transitions.

The main contributions of this paper are summarized as follows:

(i) Unlike numerous studies in the existing literature that utilize LQI frameworks with fixed optimal gains, this research develops an Adaptive Online LQI control system that dynamically updates its parameters under varying road and velocity conditions.
(ii) A hybrid optimization–adaptation framework is established where a PSO-based offline initialization process guarantees the optimal baseline Q and R weighting matrices for the LQI controller before vehicle deployment, ensuring performance enhancement in the resulting control outputs.
(iii) The proposed control strategy incorporates a dual-layer active estimation scheme using an FFRLS algorithm and a Kalman–Bucy filter to estimate cornering stiffnesses and vehicle side-slip angle. These real-time estimations are integrated into the control loop, thereby ensuring an adaptive operational structure for the overall system.
(iv) High-precision path tracking under aggressive maneuvers is achieved by integrating the adaptive online LQI controller with Stanley geometric control approach.
(v) The proposed Adaptive Online LQI controller was validated to exhibit superior performance compared to both conventional LQI and other control systems in the MATLAB/Simulink R2024b and IPG CarMaker co-simulation environment.

The remainder of this paper is organized as follows: Section 2 introduces the autonomous vehicle models employed throughout the paper. Section 3 elaborates on the systematic synthesis of the proposed path tracking control system. In Section 4, the efficacy of the integrated controller is rigorously validated through extensive MATLAB/Simulink and IPG CarMaker co-simulations. Finally, Section 5 provides concluding remarks by synthesizing the core findings and identifying potential directions for future work.

2. Autonomous Vehicle Models

This study incorporates both linear and nonlinear autonomous vehicle models for the controller design and realistic system representation. While the linear model isemployed to design and implement the optimal control strategy, the nonlinear IPG CarMaker model is used as the testing environment. Similar vehicle modelling approaches can be found in [1–5,14,28,29]. Furthermore, a linear tire model is integrated into the linear control system

synthesis, while the high-fidelity Magic Formula is utilized in the simulation environment to represent realistic tire–road interactions.

2.1. Nonlinear Autonomous Vehicle Path Tracking Model

This section introduces a 2-DOF single-track vehicle model which incorporates coupled longitudinal and lateral dynamic equations for the control architecture. The proposed control strategies are synthesized and initially validated using this modeling framework. Figure 1 illustrates the single-track vehicle dynamics integrated with the reference trajectory intended for tracking.

The governing equations for the longitudinal and lateral vehicle dynamics, incorporating the vehicle yaw motion equation, are defined as follows:

$$m(\dot{V}_x - \dot{\psi}V_y) = \sum_{i=f,r} (F_{xi}\cos\delta_i - F_{yi}\sin\delta_i) \tag{1}$$

$$m(\dot{V}_y + \dot{\psi}V_x) = \sum_{i=f,r} (F_{xi}\sin\delta_i + F_{yi}\cos\delta_i) \tag{2}$$

$$I_z\ddot{\psi} = l_aF_{yf}\cos\delta_f - l_bF_{yr}\cos\delta_r + l_aF_{xf}\sin\delta_f - l_bF_{xr}\sin\delta_r \tag{3}$$

In these equations, V_x and V_y denote the longitudinal and lateral velocities of the vehicle, respectively. The yaw angle is denoted by ψ, with $\dot{\psi}$ defining the yaw rate and $\ddot{\psi}$ signifying the yaw acceleration. The geometric parameters l_a and l_b specify the distances from the vehicle's center of gravity (CG) to the front and rear axles, respectively. Furthermore, δ_f and δ_r represent the steering angles of the front and rear wheels. Here, a front wheel steering vehicle is considered so δ_r is taken as zero.

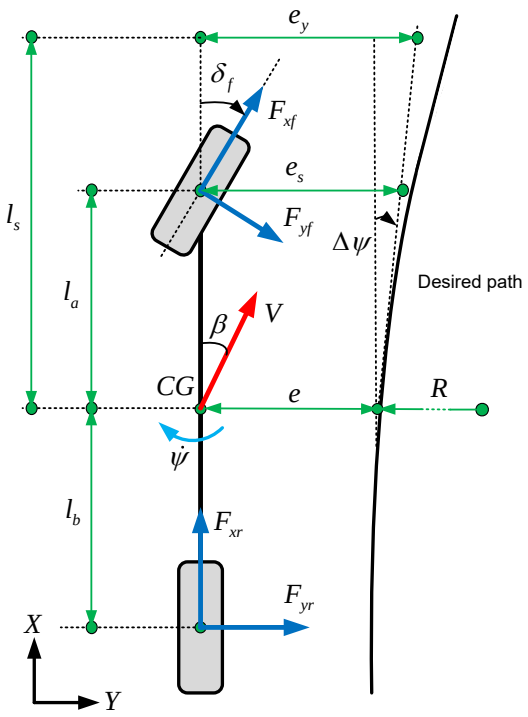

Figure 1. Vehicle path tracking model.

The tire slip angles for the front and rear tires, denoted by α_f and α_r, are calculated based on the vehicle's planar motion variables and the respective steering inputs, as given by the following equations:

$$\alpha_f = \delta_f - \arctan\left(\frac{V_y + l_a\dot{\psi}}{V_x}\right) \tag{4}$$

$$\alpha_r = \delta_r - \arctan\left(\frac{V_y - l_b\dot{\psi}}{V_x}\right) \tag{5}$$

The lateral deviation rate of the vehicle with respect to the road center line at the center of gravity, denoted by $\dot{e}$, can be expressed by incorporating the longitudinal and lateral velocity components as follows:

$$\dot{e} = V_x \sin\Delta\psi + V_y \cos\Delta\psi \tag{6}$$

The yaw angle error dynamics are characterized by its time derivative, which quantifies the discrepancy between the vehicle's angular motion and the road's geometric path. This rate of change is formulated as the difference between the vehicle's yaw rate, $\dot{\psi}$, and the steady-state desired yaw rate for turning the path. In this context, V denotes the total vehicle speed, while the road's geometric characteristics are represented by the radius R or the curvature ρ, where $\rho = 1/R$. The equation for the time derivative of the yaw angle error, $\Delta\dot{\psi}$, is given below:

$$\Delta\dot{\psi} = \dot{\psi} - \frac{V}{R} = \dot{\psi} - V\rho \tag{7}$$

The lateral deviation of the vehicle from the desired path at the preview distance, denoted by e_y, is determined by the geometric relationship involving the lateral velocity deviation $\dot{e}_y$ and the preview distance l_s as follows:

$$e_y = e + l_s \sin\Delta\psi \tag{8}$$

2.2. Linear Autonomous Vehicle Path Tracking Model

To facilitate the control design, the nonlinear vehicle tracking dynamics are linearized under the constant vehicle speed, linear tire behavior, and small-angle assumptions. This linear vehicle model is utilized to design the optimal controller. Specifically, this approach enables the calculation of control gains for each state through the system's state-space representation. The governing equations for the system states comprising the side-slip angle (β), the yaw rate ($\dot{\psi}$), the yaw angle error ($\Delta\psi$), and the lateral deviation at the preview distance (e_y) are presented below.

$$\begin{bmatrix} \dot{\beta} \\ \ddot{\psi} \\ \Delta\dot{\psi} \\ \dot{e}_y \end{bmatrix} = \underbrace{\begin{bmatrix} a_{11} & a_{12} & 0 & 0 \\ a_{21} & a_{22} & 0 & 0 \\ 0 & 1 & 0 & 0 \\ V & l_s & V & 0 \end{bmatrix}}_{A} \begin{bmatrix} \beta \\ \dot{\psi} \\ \Delta\psi \\ e_y \end{bmatrix} + \underbrace{\begin{bmatrix} b_{11} \\ b_{21} \\ 0 \\ 0 \end{bmatrix}}_{B} \delta_f + \underbrace{\begin{bmatrix} 0 \\ 0 \\ -V \\ -l_s V \end{bmatrix}}_{B_d} \rho \tag{9}$$

where the system states are defined as $x = \begin{bmatrix} \beta & \dot{\psi} & \Delta\psi & e_y \end{bmatrix}^T$. The system inputs include the control input δ_f and the disturbance ρ. Some matrix elements written implicitly are given explicitly below:

$$\begin{cases} a_{11} = \frac{-(C_r+C_f)}{mV}, \quad a_{12} = -1 + \frac{(C_r l_b - C_f l_a)}{mV^2} \\ a_{21} = \frac{(C_r l_b - C_f l_a)}{I_z}, \quad a_{22} = \frac{-(C_f l_a^2 + C_r l_b^2)}{I_z V} \\ b_{11} = \frac{C_f}{mV}, \quad b_{21} = \frac{C_f l_a}{I_z} \end{cases} \tag{10}$$

where C_f and C_r denote the cornering stiffnesses of the front and rear axles, respectively.

2.3. Tire Models

For the synthesis of the optimal controller, a linear tire model is employed in the linear system model. The lateral tire forces are formulated using the aforementioned cornering stiffnesses and the tire slip angles:

$$F_{yi} = C_i \alpha_i, \quad i \in \{f, r\} \tag{11}$$

However, to accurately reflect the complex and nonlinear behavior of tire–road interactions during high-fidelity simulations, the tire dynamics within the IPG CarMaker environment are characterized by the Magic Formula. While the linear model provides a basis for the optimal control design, the Magic Formula ensures that the simulation results account for saturation effects and nonlinearities.

Although a linear 2-DOF single-track vehicle model is employed to construct the state-space formulation and optimal controller synthesis, all performance evaluations are conducted using a fully nonlinear, high-fidelity IPG CarMaker vehicle model. IPG CarMaker models incorporate complex engine, steering and suspension dynamics, multi-body dynamics and kinematics, dynamic load transfers, and the Magic Formula tire model, which accurately captures nonlinear tire behaviour and tire force saturation. A high-fidelity sedan vehicle model provided within the IPG CarMaker environment is utilized for the simulations. The physical properties of the this vehicle, along with the specific simulation parameters employed throughout the study, are detailed in Table 1.

Table 1. Vehicle and simulation parameters used in the study.

Parameters	Description	Value	Unit
m	Vehicle mass	1619.96	kg
I_z	Yaw moment of inertia	2253.8	kg·m^2
l_a	Distance from CoG to front axle	1.075	m
l_b	Distance from CoG to rear axle	1.715	m
C_f	Front axle cornering stiffness	252,000	N/rad
C_r	Rear axle cornering stiffness	188,000	N/rad
l_s	Preview distance	15	m
μ	Tire–road friction coefficient	1	–

3. Path Tracking Control System Design

This section details the control systems developed to ensure precise path tracking. Alongside conventional methodologies, this study introduces innovative control approaches including Adaptive Online Linear Quadratic Integral (AOLQI) control. The control framework further integrates a Stanley controller, a Forgetting Factor Recursive Least Squares (FFRLS) algorithm for tire cornering stiffness estimation, and a Kalman–Bucy filter for accurate side-slip angle estimation. The proposed novel control strategy is described in detail, highlighting its distinct advantages over existing methods.

Figure 2 shows the proposed control system architecture. The framework integrates an offline PSO optimization stage to determine optimal weighting matrices of AOLQI control

system. During real-time operation, a dual-layer estimation module (FFRLS algorithm and Kalman–Bucy filter) provides instantaneous estimations to the hybrid AOLQI and Stanley controller, which computes the final steering command (δ_f) for the high-fidelity CarMaker vehicle model. Automated vehicle model block provides the lateral tire forces (F_{yf}, F_{yr}), tire slip angles (α_f, α_r), yaw angle (ψ), yaw angle error ($\Delta\psi$), yaw rate ($\dot{\psi}$), vehicle velocity (V) and lateral deviation at the center of the gravity (e) to the estimation and control layers. The vehicle side-slip angle ($\hat{\beta}$), and cornering stifnesses ($\hat{C}_f, \hat{C}_r$) are estimated in the estimation layer which are then fed into the control layer. Table 2 shows the simulation signals and their sources.

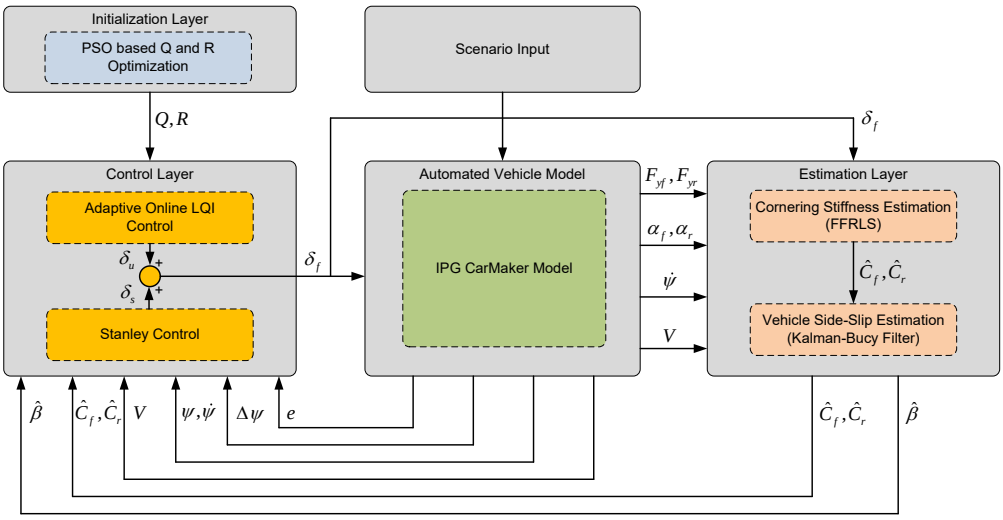

Figure 2. Integrated AOLQI-Stanley path tracking control system architecture with tire cornering stiffness and side-slip angle.

Table 2. Signal descriptions and sources.

Symbol	Description	Source
F_{yf}, F_{yr}	Lateral tire forces	IPG CarMaker output
α_f, α_r	Tire slip angles	IPG CarMaker output
$\psi, \dot{\psi}$	Vehicle yaw angle and yaw rate	IPG CarMaker output
V	Vehicle velocity	IPG CarMaker output
$\Delta\psi$	Vehicle yaw angle error	Calculated using (7)
e	Lateral deviation of the vehicle from the desired path at the vehicle CG	IPG CarMaker output
e_y	Lateral deviation of the vehicle from the desired path at the preview distance	Calculated using (8)
e_s	Cross-track error of the vehicle on the front axle	Calculated using (43)
$\hat{C}_f, \hat{C}_r$	Estimated cornering stiffness values	Calculated using (23)–(26)
$\hat{\beta}$	Estimated vehicle-side slip angle	Calculated using (27)–(32)
δ_u	AOLQI control signal	Calculated using (20)–(22)
δ_s	Stanley controller steering command	Calculated using (42)–(44)
δ_f	Total front-wheel steering command	Calculated using (45)

In real-world vehicle applications, longitudinal vehicle speed can be obtained via wheel speed sensors. IMU longitudinal acceleration, yaw rate and lateral acceleration can

be measured using a standard IMU. Steering angle can be obtained from a steering angle sensor. These standard signals can be read directly via CAN-Bus. The lateral deviation of the vehicle from the desired path can be derived from onboard perception and navigation modules, such as GNSS and camera systems.

3.1. Linear Quadratic Integral (LQI) Control Systems

To optimize the path tracking performance of the autonomous vehicle, a Linear Quadratic Integral (LQI) control architecture can be utilized [5,14,29,30]. This section details the transition from classical LQR to the augmented integral structure and the selection of weighting parameters. The standard LQR approach is highly effective for regulation but often suffers from eliminating steady-state errors for reference tracking.

To address this, an integral state $z(t)$ is introduced based on the lateral deviation at the preview distance e_y:

$$\begin{cases} e(t) = e_{y,ref}(t) - e_y(t) \\ \dot{z}(t) = e(t) \end{cases} \tag{12}$$

By augmenting the original linear vehicle states $x(t) = [\beta \quad \dot{\psi} \quad \Delta\psi \quad e_y]^T$ with this integral term, the augmented state vector $\bar{x}$ and the corresponding system dynamics are defined as:

$$\bar{x}(t) = \begin{bmatrix} \beta & \dot{\psi} & \Delta\psi & e_y & z \end{bmatrix}^T \tag{13}$$

$$\begin{bmatrix} \dot{x}(t) \\ \dot{z}(t) \end{bmatrix} = \underbrace{\begin{bmatrix} A & \mathbf{0}_{4\times 1} \\ -C & 0 \end{bmatrix}}_{\bar{A}} \begin{bmatrix} x(t) \\ z(t) \end{bmatrix} + \underbrace{\begin{bmatrix} B \\ 0 \end{bmatrix}}_{\bar{B}} u(t) \tag{14}$$

where A and B are defined in (9), and $C = [0 \quad 0 \quad 0 \quad 1]$ is the output matrix used to extract the lateral deviation. The LQI controller determines the optimal steering input $u = \delta_u$ by minimizing the following quadratic cost function:

$$J_{LQI} = \int_0^\infty (\bar{x}(t)^T Q \bar{x}(t) + u(t)^T R u(t))dt \tag{15}$$

The optimal control law is formulated as a state-feedback gain:

$$u(t) = -K\bar{x}(t) = -[K_{LQR} \quad K_I] \begin{bmatrix} x(t) \\ z(t) \end{bmatrix} \tag{16}$$

The gain matrix K is computed by solving the Algebraic Riccati Equation (ARE):

$$\bar{A}^T P + P\bar{A} - P\bar{B}R^{-1}\bar{B}^T P + Q = 0 \tag{17}$$

$$K = R^{-1}\bar{B}^T P \tag{18}$$

The weighting matrices, Q and R, are crucial in determining an ideal balance between path tracking accuracy and steering maneuver comfort. The state weighting matrix, Q, is constructed as a diagonal matrix, with the initial four members representing the fundamental states of the original linear vehicle model and the last one is the integral error state:

$$Q = \mathrm{diag}(q_\beta, q_{\dot{\psi}}, q_{\Delta\psi}, q_{e_y}, q_z) \tag{19}$$

Within this framework, the integral error state (z) is explicitly penalized to eradicate steady-state offsets, hence guaranteeing precise tracking. In contrast, the control effort weighting, R, is a scalar quantity that signifies the penalty applied to the front steering

angle. This penalty is essential for preventing excessive actuator responses and maintaining the dynamic stability of the steering system.

3.2. Adaptive Online LQI (AOLQI) Control Systems

The Adaptive Online Linear Quadratic Integral (AOLQI) control architecture enhances the conventional LQI law by integrating real-time parameter estimation and state observation mechanisms. Departing from the use of static nominal values, the system matrices, $\bar{A}$ and $\bar{B}$, are dynamically recalculated online to reflect the vehicle's instantaneous dynamics. The front and rear tire cornering stiffnesses (C_f, C_r) exhibit significant variability under fluctuating road conditions and vertical load transfers. To estimate these variables, a Forgetting Factor Recursive Least Squares (FFRLS) estimator is implemented. Furthermore, since the side-slip angle (β) is difficult and cost-prohibitive to measure directly in mass production vehicles, a Kalman–Bucy Filter (KF) is designed to estimate the side-slip angle. This filter uses yaw rate, velocity measurements and cornering stiffness estimations to provide side-slip angle estimation. As a result of this integration, the AOLQI framework is formulated as a continuous-time linear time-varying (LTV) system, where the state-space matrices are explicit functions of the instantaneous velocity (V) and the estimated parameters ($\hat{C}_f, \hat{C}_r$):

$$\dot{\bar{x}}(t) = \bar{A}(t)\bar{x}(t) + \bar{B}(t)u(t) \tag{20}$$

The time-varying nature of the system matrices is expressed as follows:

$$\begin{cases} \bar{A}(t) = f(V(t), \hat{C}_f(t), \hat{C}_r(t)) \\ \bar{B}(t) = g(V(t), \hat{C}_f(t)) \end{cases} \tag{21}$$

The proposed control law is dynamically computed at each time step by solving the Algebraic Riccati Equation (ARE) for the updated system matrices:

$$u(t) = \delta_u(t) = -K(t)\bar{x}(t) \tag{22}$$

where $K(t)$ represents the time-varying controller gain matrix.

3.3. Forgetting Factor Recursive Least Squares (FFRLS) Algorithm

Vehicle parameters, particularly the front and rear cornering stiffness values (C_f, C_r), exhibit significant variations due to changes in tire–road friction and vertical load transfer. To ensure the LQI controller operates with high fidelity, a Forgetting Factor Recursive Least Squares (FFRLS) algorithm is implemented for real-time cornering stiffness estimation. The estimation model is derived from the vehicle's lateral and yaw dynamics. By discretizing the equations of motion as shown in (11), the system is expressed in a standard regression form [18]:

$$y(k) = \varphi^T(k)\theta(k) + \xi(k) \tag{23}$$

where $y(k)$ represents the measured lateral tire force, $\varphi(k)$ is the regression vector containing tire slip angles, $\theta(k) = [C_f, C_r]^T$ is the vector of unknown parameters to be estimated, and $\xi(k)$ denotes the measurement noise. The FFRLS algorithm updates the parameter estimates at each time step k using the following recursive equations:

$$\hat{\theta}(k) = \hat{\theta}(k-1) + K(k)[y(k) - \varphi^T(k)\hat{\theta}(k-1)] \tag{24}$$

$$K(k) = \frac{P(k-1)\varphi(k)}{\lambda + \varphi^T(k)P(k-1)\varphi(k)} \tag{25}$$

$$P(k) = \frac{1}{\lambda}[I - K(k)\varphi^T(k)]P(k-1) \tag{26}$$

Here, $K(k)$ denotes the recursive gain matrix, $P(k)$ is the covariance matrix initialized as $P(0) = 1000 \cdot I_{2\times2}$, and $\lambda \in (0,1]$ is the forgetting factor. A typical value 0.995 is selected to balance tracking convergence and noise attenuation. In (23), the regression vector $\varphi(k) = [\alpha_f(k), \alpha_r(k)]^T$ explicitly separates the front and rear tire dynamics based on the front and rear slip angles (α_f, α_r). Since $\alpha_f = \delta_f - \beta - \frac{l_a\dot{\psi}}{V_x}$, whereas $\alpha_r = \delta_r - \beta + \frac{l_b\dot{\psi}}{V_x}$ in linear form, $\varphi(k)$ retains linear independence during steering transients. This allows the covariance matrix $P(k)$ in (25) to independently update the gain vector $K(k)$, thereby decoupling the online identification of $\hat{C}_f$ and $\hat{C}_r$. To prevent covariance wind-up during low-lateral excitation driving (e.g., straight roads), a conditional dead-zone mechanism is integrated into the FFRLS algorithm. Parameter adaptation only occurs when the threshold levels are surpassed. Furthermore, projection bounds $\hat{C}_{f,r} \in [C_{f,r,\min}, C_{f,r,\max}]$ are enforced to ensure physical plausibility in all operating conditions.

The lateral tire forces (F_{yf}, F_{yr}) and tire slip angles (α_f, α_r) exported directly from IPG CarMaker in the simulation setup to evaluate ideal convergence rates. From a practical implementation perspective, the inputs required for the FFRLS estimator do not rely on direct wheel force transducers; instead, the lateral force $y(k)$ is reconstructed via yaw rate and lateral acceleration measurements alongside vehicle lateral and yaw motion equations, and tire slip angles are computed using front wheel steering angle, yaw rate, longitudinal velocity measurements and the estimated side-slip angle from the Kalman–Bucy filter.

The estimated cornering stiffness values, $\hat{C}_f$ and $\hat{C}_r$, are subsequently fed into the time-varying system matrices $\bar{A}(k)$ and $\bar{B}(k)$. This allows the LQI controller to compute optimal gains dynamically, effectively compensating for tire–road condition changes and maintaining high path tracking precision.

3.4. Kalman–Bucy Filter (KF)

The Kalman–Bucy Filter (KF) is the continuous-time version of the original discrete-time Kalman filter, which is an optimal filter that minimizes the mean squared error [7,31]. It is implemented here to estimate the side-slip angle (β), which is typically not directly measurable with standard production sensors. The yaw rate, velocity measurements and cornering stiffness estimations are employed as the inputs to the KF.

The vehicle dynamics model for KF design are shown in a continuous-time state-space representation, where the KF model matrices are updated online using the velocity measurement (V), the cornering stiffness estimations $(\hat{C}_f, \hat{C}_r)$:

$$\dot{x}_e(t) = A_e(t)x(t) + B_e(t)u_e(t) + G_e(t)w(t) \tag{27}$$

$$y_e(t) = C_e(t)x_e(t) + v(t) \tag{28}$$

Here, the state vector is defined as $x_e(t) = [\beta \quad \dot{\psi}]^T$, the control input $u_e(t)$ is the front steering angle δ_f and the output $y_e(t)$ is the yaw rate $\dot{\psi}$, where $C_e = [0 \quad 1]$, and $G_e = 1$. The time-varying system matrices $A_e(t)$ and $B_e(t)$ are updated based on the following matrix elements:

$$\begin{cases} a_{11} = -\frac{\hat{C}_f+\hat{C}_r}{mV}, a_{12} = -1 + \frac{l_b\hat{C}_r - l_a\hat{C}_f}{mV^2} \\ a_{21} = \frac{l_b\hat{C}_r - l_a\hat{C}_f}{I_z}, a_{22} = -\frac{l_a^2\hat{C}_f + l_b^2\hat{C}_r}{I_zV} \\ b_{11} = \frac{\hat{C}_f}{mV}, b_{21} = \frac{l_a\hat{C}_f}{I_z}. \end{cases} \tag{29}$$

The process noise $w(t)$ and measurement noise $v(t)$ are modeled as zero-mean Gaussian white noise processes (with the measurement noise power configured as 1×10^{-6} at a sample time of 0.1 s). To enhance estimation accuracy, the stochastic properties of these noises are empirically determined by analyzing noise samples from the lateral acceleration measurement. This sensor-based characterization enabled the precise calibration of the covariance matrices $Q_e = \mathrm{diag}(0.02, 0.3)$ and $R_e = 1 \times 10^{-7}$ (with zero cross-covariance $N = 0$). Assuming no cross-correlation between process and measurement noise, the optimal state estimate $\hat{x}_e(t)$ is generated as follows:

$$L = PC_e^T R_e^{-1} \tag{30}$$

$$\dot{P} = A_e P + PA_e^T + G_e Q G_e^T - LR_e L^T \tag{31}$$

$$\dot{\hat{x}}_e = A_e \hat{x}_e + B_e u_e + L(y_e - C_e \hat{x}_e) \tag{32}$$

This adaptive framework allows the filter to track varying road conditions in real-time, ensuring precise state estimation for the subsequent control stages.

To mathematically establish the reliability of the proposed co-simulation framework, we present a unified closed-loop system stability and boundedness analysis. By applying a physical projection operator to the FFRLS algorithm [32], the estimated cornering stiffnesses are strictly constrained within known lower and upper physical limits: $\hat{C}_i(t) \in [C_{i,\min}, C_{i,\max}] = [100{,}000, 600{,}000]$ N/rad for $i \in \{f, r\}$. This guarantees that all entries of the time-varying state-space matrices $\bar{A}(t)$ and $\bar{B}(t)$ remain bounded at all times.

Since the vehicle side-slip angle $\beta(t)$ is estimated online as $\hat{\beta}(t)$ by a continuous-time Kalman–Bucy filter, the convergence of the estimator error must be ensured [33]. Assuming the vehicle maintains a non-zero velocity ($V(t) \geq V_{min} > 0$), the continuous time-varying system matrices $(A_e(t), C_e(t))$ satisfy the uniform complete observability condition over an interval $[t, t + T_s]$. Consequently, for strictly positive-definite process and measurement noise covariance matrices, the Riccati covariance matrix $P(t)$ of the Kalman–Bucy filter is uniformly bounded. This uniform boundedness guarantees exponentially stable error dynamics with bounded estimation error variance in the sense of Kalman–Bucy filtering theory.

For the linear time-varying (LTV) error dynamics $\dot{e}(t) = A_{cl}(t)e(t) + \bar{B}(t)\delta_s(e,t)$, where $A_{cl}(t) = \bar{A}(t) - \bar{B}(t)K(t)$, we define a time-varying quadratic Lyapunov candidate function:

$$V(e(t), t) = \frac{1}{2} e^T(t) P(t) e(t) \tag{33}$$

where $P(t) = P^T(t) > 0$ is the unique symmetric positive-definite matrix solution of the continuous-time algebraic Riccati Equation recalculated online at each time instant t:

$$\bar{A}^T(t)P(t) + P(t)\bar{A}(t) - P(t)\bar{B}(t)R^{-1}\bar{B}^T(t)P(t) + Q = 0 \tag{34}$$

Rearranging the Riccati equation with $K(t) = R^{-1}\bar{B}^T(t)P(t)$ yields the symmetric closed-loop Lyapunov relation:

$$A_{cl}^T(t)P(t) + P(t)A_{cl}(t) = -Q_{cl}(t) \tag{35}$$

where $Q_{cl}(t) = Q + K^T(t)RK(t) > 0$. Taking the total time derivative of $V(e(t), t)$ along the trajectory of the perturbed time-varying system gives:

$$\dot{V}(e(t), t) = \frac{1}{2} e^T(t) \Big(A_{cl}^T(t)P(t) + P(t)A_{cl}(t) \Big) e(t) + \frac{1}{2} e^T(t) \dot{P}(t) e(t) + e^T(t) P(t) \bar{B}(t) \delta_s(e,t) \tag{36}$$

Substituting the Lyapunov relation into the derivative yields:

$$\dot{V}(e(t),t) = -\frac{1}{2}e^T(t)Q_{cl}(t)e(t) + \frac{1}{2}e^T(t)\dot{P}(t)e(t) + e^T(t)P(t)\bar{B}(t)\delta_s(e,t) \tag{37}$$

Since vehicle parameters $(V(t), \hat{C}_f(t), \hat{C}_r(t))$ vary continuously within bounded physical envelope limits, the time derivative of the Riccati solution matrix is upper-bounded by $\|\dot{P}(t)\| \leq \epsilon_p < \infty$. Furthermore, the geometric Stanley control component $\delta_s(e,t)$ is Lipschitz continuous with bound $\|\delta_s(e,t)\| \leq L_s\|e(t)\|$. Applying the Rayleigh–Ritz theorem and Cauchy–Schwarz inequality:

$$\dot{V}(e(t),t) \leq -\left(\frac{1}{2}\lambda_{\min}(Q_{cl}(t)) - \frac{1}{2}\epsilon_p - \|\bar{B}(t)\|\|P(t)\|L_s\right)\|e(t)\|^2 \tag{38}$$

Provided that the control weighting matrices Q and R are selected such that $\lambda_{\min}(Q_{cl}(t)) > \epsilon_p + 2\|\bar{B}(t)\|\|P(t)\|L_s$, the derivative satisfies $\dot{V}(e(t),t) < 0$, guaranteeing Uniform Asymptotic Stability of the integrated closed-loop system [34,35]. Here, $\lambda_{\min}(Q_{cl})$ denotes the minimum eigenvalue of a symmetric positive-definite matrix Q_{cl}.

3.5. Particle Swarm Optimization (PSO) Algorithm

In this study, the Particle Swarm Optimization (PSO) algorithm is employed as an offline meta-heuristic optimization tool to determine the weighting matrices Q and R of the LQI controller. Unlike trial-and-error tuning, PSO identifies the optimal weighting parameters that minimize the cost function before the Adaptive Online LQI (AOLQI) phase begins. This ensures that the controller starts the adaptive online process with an ideal gain K.

The Particle Swarm Optimization (PSO) algorithm is utilized as a meta-heuristic tool to explore the continuous search space of the weighting parameters. By simulating the collective social behavior of a swarm, PSO identifies the optimal baseline configurations for the controller. In this framework, each particle i represents a candidate solution within the parameter space. These particles dynamically adjust their trajectories toward the optimal solution by leveraging their personal best positions (p_{best}) and the global best position (g_{best}) discovered by the entire swarm. The velocity and position update laws for each particle i in a specific dimension d are formulated as follows [14–16,29]:

$$\begin{aligned} v_{i,d}(k+1) = \omega v_{i,d}(k) &+ c_1 r_1(p_{best_{i,d}} - s_{i,d}(k)) \\ &+ c_2 r_2(g_{best_d} - s_{i,d}(k)) \end{aligned} \tag{39}$$

$$s_{i,d}(k+1) = s_{i,d}(k) + v_{i,d}(k+1) \tag{40}$$

where i denotes the particle index, d represents the dimension of the parameter space (corresponding to the diagonal elements of the weighting matrices), and k signifies the iteration count. The velocity component $v_{i,d}$ dictates the search direction and step size, while $s_{i,d}$ defines the current candidate weight value. The trade-off between global exploration and local exploitation is governed by the inertia weight ω, which is complemented by the cognitive (c_1) and social (c_2) acceleration coefficients. Furthermore, r_1 and r_2 are independent random variables uniformly distributed in the range $[0,1]$.

In the proposed framework, the optimal weight matrices Q and R are determined by minimizing a quantitative cost function J_{PSO} using the PSO algorithm. Specifically, each particle in the PSO algorithm represents a candidate parameter vector $\sigma = [q_\beta, q_{\dot{\psi}}, q_{\Delta\psi}, q_{e_y}, q_z, r]^T$, which constructs the diagonal elements of the weighting matrices $Q = \text{diag}(q_\beta, q_{\dot{\psi}}, q_{\Delta\psi}, q_{e_y}, q_z)$ and $R = r$. The optimality of these matrices is character-

ized by the minimization of the integral performance metric over a finite time horizon T, which is defined as follows:

$$J_{PSO}(\sigma) = \int_0^T \left(q_\beta \beta^2(t) + q_{\dot{\psi}} \dot{\psi}^2(t) + q_{\Delta\psi} \Delta\psi^2(t) + q_{e_y} q_{\dot{e}_y}^2(t) + q_z q_z^2(t) + r {\delta_u}^2(t) \right) dt \quad (41)$$

The matrices Q^* and R^* are declared optimal when the PSO algorithm converges to the global minimum of $J_{PSO}(\sigma)$, thereby guaranteeing an optimal trade-off between minimizing path-tracking deviations and preventing excessive control saturation.

In this study, the PSO is configured with a population of 50 particles over 1000 iterations. The optimization process is initialized with Q and R as identity matrices to ensure a neutral starting point. Furthermore, the search space for the diagonal elements of the Q matrix and the R weighting parameter is bounded within the lower limit of $\mathrm{lb} = [1, 1, 1, 1, 1]$ and the upper limit of $\mathrm{ub} = [5, 5, 5, 5, 5]$. The resulting optimized baseline weights are subsequently passed to the AOLQI control module, where the FFRLS algorithm and Kalman–Bucy filter provide real-time updates of the tire cornering stiffness and the side-slip angle values. The specific optimized values for Q and R are detailed in the simulation results section.

3.6. Stanley Control System

The Stanley controller is a well-established geometric steering strategy that employs a nonlinear control law for path tracking. This architecture is specifically utilized to minimize cross-track error and yaw angle error by computing the optimal front steering angle. Integrating the Stanley framework into the proposed AOLQI system aims to leverage these geometric advantages to further suppress lateral deviations and enhance path tracking accuracy.

The Stanley control law computes the steering command based on front-axle kinematics. To enhance path tracking performance during extreme maneuvers, this formulation is augmented with yaw rate and steering rate damping terms. By incorporating these dynamic enhancements, the modified control architecture ensures superior path tracking precision within complex driving scenarios. The augmented Stanley steering command, denoted by $\delta_s(t)$, can be written as follows [20]:

$$\begin{aligned} \delta_s(t) =& (\psi(t) - \psi_{ss}(t)) + \arctan\left(\frac{k_y e_s(t)}{k_{soft} + V(t)} \right) \\ &+ k_{d,yaw}(\dot{\psi} - V\rho) + k_{d,steer}\dot{\delta}(t) \end{aligned} \quad (42)$$

where the cross-track error based on the front axle, denoted by e_s, can be calculated by using the results of (6) as follows:

$$e_s = e + l_f sin(\Delta\psi) \quad (43)$$

and the steady-state yaw angle can be determined as:

$$\psi_{ss} = \frac{mV^2\rho}{C_f(1 + \frac{l_a}{l_b})}. \quad (44)$$

In (42), the constant k_y is the gain coefficient, while the denominator includes the vehicle velocity $V(t)$ to adapt the steering sensitivity. Furthermore, $k_{d,yawrate}$ and $k_{d,steer}$ are the differential damping gains specifically designed to suppress high-frequency oscillations and ensure steering smoothness by penalizing the yaw rate error $(\dot{\psi} - V\rho)$ and the steering angle rate $(\dot{\delta}(t))$, k_{soft} is a softening constant used to prevent numerical instability at very

low speeds, respectively. After the inclusion of the Stanley controller, the total control signal can be obtained.

The integrated control framework combines the regulation capability of the AOLQI controller with the geometric path tracking performance of the Stanley controller in a continuous parallel configuration. Specifically, the total front-wheel steering command $\delta_f(t)$ is formed by the direct linear superposition of the individual control signals, rather than through discrete switching or dynamic weight allocation:

$$\delta_f(t) = \delta_u(t) + \delta_s(t) \tag{45}$$

Since both control components generate continuous outputs, their direct summation ensures a smooth steering profile without abrupt actuator jumps or chattering, thereby preserving ride comfort and mechanical durability.

3.7. Adaptive Online LQI-Stanley Integrated Control System (AOLQI+PSO+Stanley)

An adaptive online LQI (AOLQI) system is developed by leveraging a conventional LQI framework integrated with a Forgetting Factor Recursive Least Squares (FFRLS) and a Kalman–Bucy Filter (KF), as detailed in the preceding sections. To enhance the control performance, the weighting matrices of this AOLQI control system are optimized offline using a Particle Swarm Optimization (PSO) algorithm, ensuring that the controller operates with optimal control gains before real-time execution. To further improve high-speed maneuverability and minimize lateral deviations during aggressive transients, a Stanley control law is integrated into the online architecture. The fusion of these components resulted in the high-precision adaptive online LQI-Stanley integrated control system (AOLQI+PSO+Stanley). The path tracking performance of this proposed architecture is benchmarked against the reference LQI, standalone AOLQI, and PSO-optimized AOLQI control systems.

The distinguishing feature of the proposed control system is the seamless integration of optimal control with Stanley algorithm to achieve high-fidelity path tracking control. This hybrid architecture, designated as AOLQI+PSO+Stanley, uniquely synthesizes offline global optimization with real-time parameter adaptation. The system architecture is characterized by a multi-layered synchronization of three distinct modules: the Initialization Layer (PSO), the Estimation Layer (FFRLS & KF), and the Control Layer (AOLQI & Stanley). The interactions between these layers and the overall control framework are illustrated in Figure 2.

The real-time feasibility of this framework is an important consideration. Since the proposed AOLQI controller updates the vehicle state-space matrices $\bar{A}(t)$ and $\bar{B}(t)$ online based on the estimated cornering stiffnesses $(\hat{C}_f, \hat{C}_r)$, the Algebraic Riccati Equation (ARE) must be solved at each sampling interval $\Delta t = 1$ ms. The ARE is formulated for an augmented 5-state system. Solving this 5×5 system using the Schur decomposition method requires a minimal number of floating-point operations. In addition, a threshold-based update mechanism is implemented to guarantee the real-time execution feasibility. The online ARE algorithm is executed to recalculate the controller gains only when the variation in the vehicle velocity exceeds a predefined threshold (0.5 m/s) relative to the velocity at the last calculation instance.

To analyze the execution time of MATLAB/Simulink and IPG CarMaker co-simulation, a comprehensive profile was performed using the Simulink Profiler during an end-to-end simulation with over 60,005 control steps and 121,815 solver sub-steps. A Windows PC with a 13th generation Intel Core i7 processor and 16 GB of RAM was used for this test. Empirical execution time metrics measured via the Simulink Profiler over an end-to-end driving cycle are summarized in Table 3.

Table 3. Measured simulation execution times per step for individual algorithmic components ($T_s = 1$ ms).

Algorithmic Component	Total Execution Time (s)	Total Calls	Execution Time per Step (ms)	Duty Cycle of 1 ms Budget
FFRLS estimator	0.316	121,815	0.0026	0.26%
Kalman–Bucy filter	1.484	121,815	0.0122	1.22%
AOLQI controller	0.236	121,815	0.0019	0.19%
Total pure control and estimation math execution	2.036	121,815	0.0167	1.67%
Overall controller and estimator subsystem (incl. signal routing and bus packaging)	6.970	60,005	0.1160	11.60%

The total pure core control and estimation algorithm (0.0167 ms) utilizes less than 1.67% of the available 1 ms sampling window. Even when accounting for full IPG CarMaker signal bus packaging (0.1160 ms), the overall controller and estimator subsystem utilizes only 11.60% of the 1 ms cycle budget. Note that the Stanley controller only involves a single-line trigonometric calculation (arctan), so its computational overhead is on the nanosecond scale. Therefore, this cost is included in the total execution time of the controller and estimator subsystems. This basic analysis demonstrates the potential for real-time execution of this approach.

While advanced control techniques such as Model Predictive Control (MPC) and Deep Reinforcement Learning (DRL) have demonstrated high path tracking performance in the literature, they present distinct operational trade-offs. MPC demands significant computational power to solve constrained optimization problems at each time step, which can induce latency risks on embedded Electronic Control Units (ECUs). DRL models, despite their flexibility, suffer from sample inefficiency, high training overhead, and lack of deterministic stability guarantees required for safety-critical automotive systems. The proposed AOLQI-Stanley framework bridges this gap by delivering real-time adaptation and tracking performance with minimal computational overhead, offering an easily implementable and mathematically tractable solution for embedded autonomous driving applications.

4. Simulation Studies

In this section, the performance of the proposed adaptive online LQI-Stanley integrated control system (AOLQI+PSO+Stanley) is evaluated through extensive co-simulations conducted in the MATLAB/Simulink and IPG CarMaker environments. To rigorously account for real-world application, the simulation study incorporates Gaussian measurement noise across sensory feedback signals, as well as native steering actuator dynamics embedded within IPG CarMaker.

To demonstrate the superiority of the proposed framework, three distinct driving scenarios are executed, each targeting different aspects of path tracking control. The performance of the proposed control architecture is rigorously compared with the control methods described in Section 3, using statistical indicators such as the root mean square error (RMSE) and integrated square error (ISE) of lateral deviation values.

The initial controller gain values for the LQI and the AOLQI are determined through the offline PSO process. By minimizing the quadratic objective function J_{LQI}, the algorithm identified the optimal weighting matrices that balance path tracking precision and steering smoothness.

In conventional LQI applications, the weighting matrices Q and R are typically selected as identity matrices (I), which implies an equal weighting for all state deviations and control efforts. In order to minimize J_{LQI} cost function, the PSO algorithm is utilized to calculate the optimal diagonal elements of these matrices. The optimized weighting matrices obtained through the PSO-based initialization phase are defined as follows:

$$\begin{cases} Q_{AOLQI+PSO} = \begin{bmatrix} 2.9732 & 0 & 0 & 0 & 0 \\ 0 & 2.2036 & 0 & 0 & 0 \\ 0 & 0 & 4.4994 & 0 & 0 \\ 0 & 0 & 0 & 3.1682 & 0 \\ 0 & 0 & 0 & 0 & 4.9502 \end{bmatrix} \\ R_{AOLQI+PSO} = 4.9502 \end{cases} \tag{46}$$

The resulting optimized controller gains (K) used in the initialization phase of the simulation scenarios are presented in Table 4.

Table 4. Control gain values for the evaluated control systems.

Control System	k_1	k_2	k_3	k_4	k_5
K_{LQI}	0.6843	0.9101	1.0744	1.0692	−1.0000
$K_{LQI+PSO}$	0.5661	0.6140	0.7953	0.8637	−1.0000

4.1. Model Validation for Controller and Estimator Designs

Before evaluating the closed-loop performance of the proposed controller, a rigorous validation process is conducted by comparing the responses of the developed 2-DOF single-track vehicle model against the IPG CarMaker model in the open-loop simulation. The validation is performed under constant velocity of 15 m/s for the same maneuver, focusing on the yaw rate ($\dot{\psi}$) and side-slip angle (β) as the primary indicators of lateral vehicle dynamics.

As illustrated in Figures 3 and 4, the yaw rate and side-slip angle profiles obtained from the linear vehicle model show a very close overlap with the IPG CarMaker model in the linear region. This alignment confirms that the linear vehicle model can be used for controller and estimator design purposes.

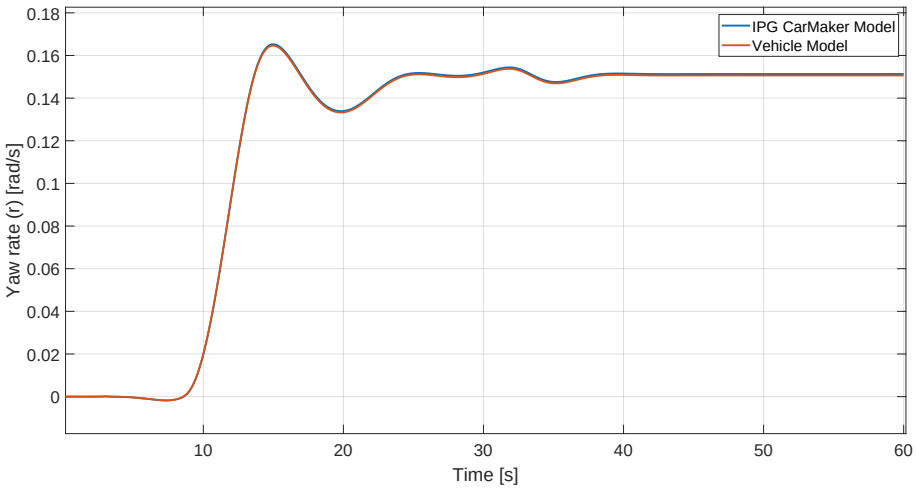

Figure 3. Yaw rate (r) response validation: Comparing the linear vehicle model and IPG CarMaker model results.

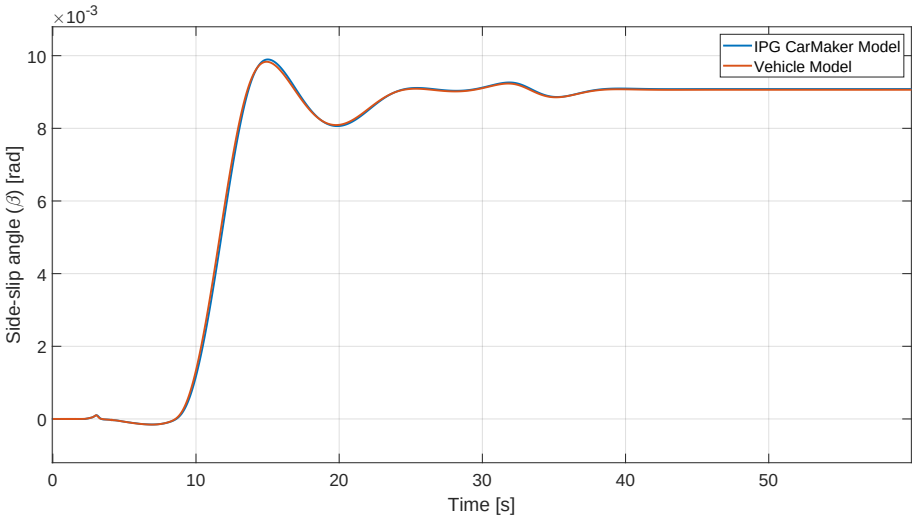

Figure 4. Side-slip angle (β) response validation: Comparing the linear vehicle model and IPG CarMaker model results.

Through the model validation process, the most accurate linear vehicle model nominal cornering stiffness values are determined as: C_f = 252,000 N/rad and C_r = 188,000 N/rad. These tuned values represent the optimal values for the linear tire region and are subsequently utilized as the nominal values for all controller and estimator design parts.

4.2. Estimation Results

The estimation of cornering stiffness parameters, $\hat{C}_f$ and $\hat{C}_r$, is conducted using the Forgetting Factor Recursive Least Squares (FFRLS) algorithm, which is configured with a forgetting factor of 0.995 to improve the steady-state convergence. The resulting estimation performance, as illustrated in Figure 5 and Figure 6, demonstrates a high degree of fidelity by successfully converging to the nominal reference values of 252,000 N/rad and 188,000 N/rad, respectively.

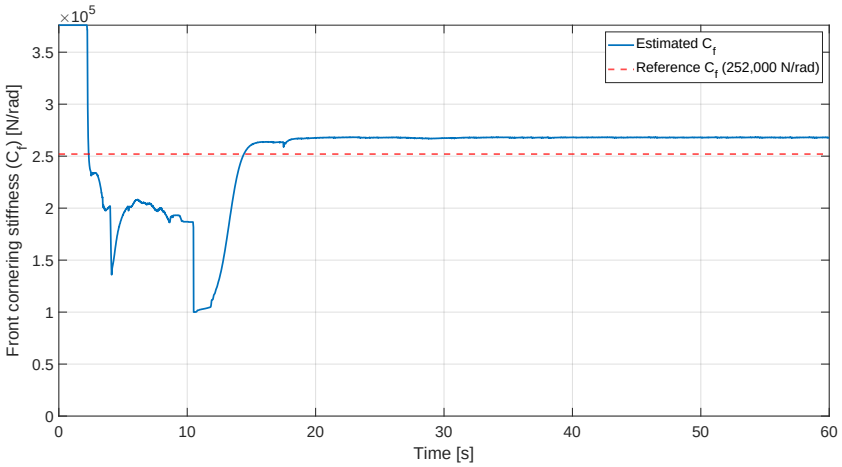

Figure 5. Estimation of the front axle cornering stiffness ($\hat{C}_f$) using the FFRLS algorithm compared to the nominal reference value.

Building upon the estimated cornering stiffness parameters, the estimation performance of the vehicle side-slip angle (β) is evaluated. As illustrated in Figure 7, the Kalman–Bucy filter exhibits successful estimation performance by effectively utilizing the real-time updated $\hat{C}_f$ and $\hat{C}_r$ values. The estimated side-slip angle shows a strong correlation with the actual side-slip angle.

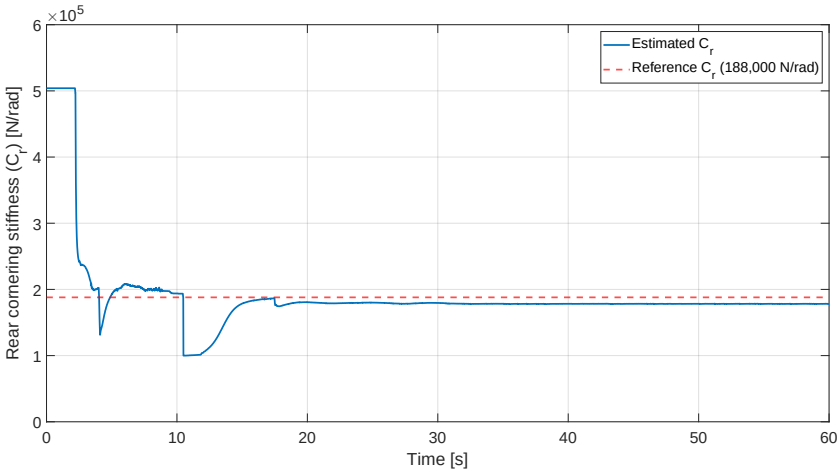

Figure 6. Estimation of the rear axle cornering stiffness ($\hat{C}_r$) using the FFRLS algorithm compared to the nominal reference value.

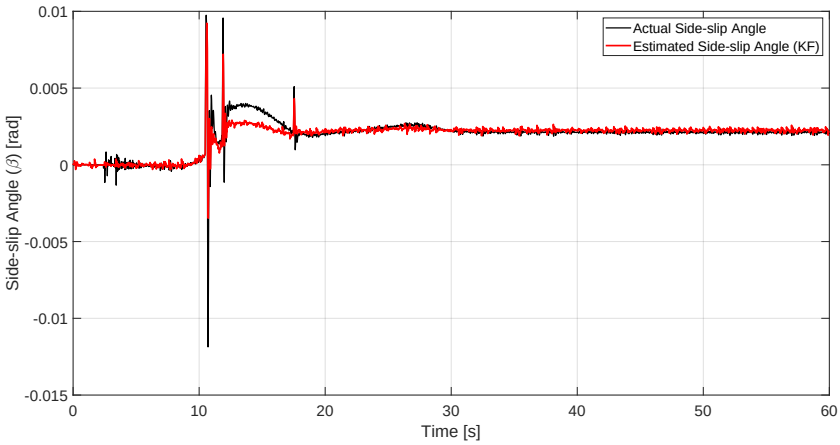

Figure 7. Side-slip angle (β) estimation performance: The Kalman–Bucy filter accurately estimates the vehicle side–slip angle by leveraging estimated cornering stiffness values.

To quantitatively validate the state estimation performance of the designed Kalman–Bucy filter, statistical error metrics for the vehicle side-slip angle (β) are summarized in Table 5. The filter exhibits exceptional tracking precision with an overall Root Mean Square Error (RMSE) of 0.000502 rad (0.0288°) and a Mean Absolute Error (MAE) of 0.000232 rad (0.0133°). Even during severe transient maneuvers ($t \approx 10 - 18$ s), the maximum estimation error is strictly bounded at 0.009889 rad (0.5666°), confirming rapid observer convergence without transient divergence. Furthermore, in the steady-state regime ($t \geq 20$ s), the steady-state RMSE drops to 0.000094 rad (0.0054°), effectively eliminating sensor noise. These quantitative findings demonstrate that the Kalman–Bucy filter provides high-fidelity, drift-free state feedback, which serves as a reliable foundation for the parameter adaptation of the AOLQI controller.

Table 5. Statistical performance metrics of the Kalman–Bucy filter for vehicle side-slip angle (β) estimation.

Performance Metric	Value (rad)	Value (deg)
Overall RMSE	0.000502	0.0288°
Overall MAE	0.000232	0.0133°
Maximum Estimation Error	0.009889	0.5666°
Steady-State RMSE ($t \geq 20$ s)	0.000094	0.0054°

4.3. Scenario 1: A 100-m Radius Circular Path Test

To rigorously evaluate the path tracking control performance, a 100-m constant radius cornering maneuver is executed within the MATLAB/Simulink and IPG CarMaker co-simulation environment, as illustrated in Figure 8. The various control strategies detailed in Section 2 are implemented and validated on this track to assess their path tracking accuracy. In order to evaluate the proposed path tracking control systems under realistic physical conditions, practical actuator constraints are introduced to the control input. The front-wheel steering angle δ_f is limited to a range of ± 0.7 rad ($\pm 40.11^\circ$) to prevent unrealistic wheel turns. These limits are indicated by red dotted lines in the results.



Figure 8. Scenario 1: A 100-m radius circular path in IPG CarMaker.

The performance of the proposed control architecture during the 100-m constant radius maneuver is illustrated in Figure 9.

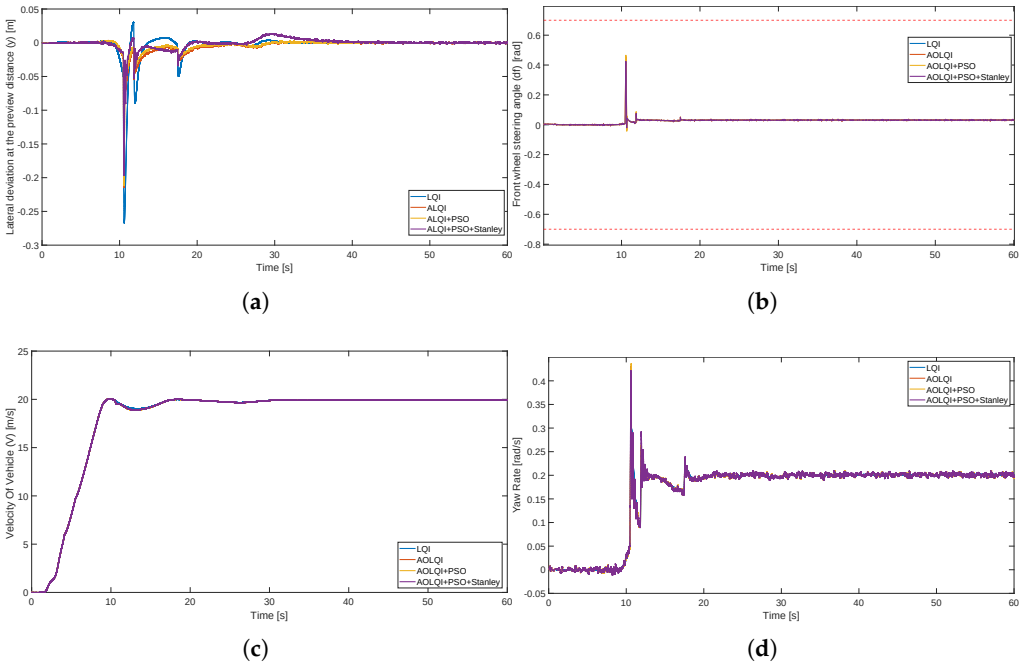

Figure 9. Simulation results for Scenario−1 (A 100 m Constant Radius Cornering): (**a**) lateral deviation at the preview distance (e_y) [m], (**b**) front wheel steering angle (δ_f) [rad], (**c**) vehicle velocity (V) [m/s], and (**d**) yaw rate ($\dot{\psi}$) [rad/s].

Regarding the lateral deviation analysis shown in Figure 9a, the proposed control framework demonstrates significantly higher path tracking performance than the conven-

tional LQI controller. By leveraging the PSO-optimized parameters in conjunction with the AOLQI and Stanley controllers, the system effectively minimizes lateral deviation and eliminates steady-state error.

The front-wheel steering angle (δ_f) responses are depicted in Figure 9b further highlight the advantages of the proposed architecture. The proposed control system maintains significantly lower peak steering magnitudes so the controller reduces the mechanical workload on the steering actuators and effectively prevents over-correction tendencies during the initial phase of the circular path transition. The desired velocity profile is successfully followed throughout the maneuver by all control systems, as shown in Figure 9c. The yaw rate response shown in Figure 9d demonstrates favorable behaviour within the established limits for vehicle yaw stability and occupant comfort across all evaluated control schemes. However, the proposed system exhibits a slightly more dampened response at the peak.

4.4. Scenario 2: Hockenheim Race Track Test

The second evaluation scenario in Figure 10 utilizes Hockenheim race track defined in the IPG CarMaker environment to assess the controller's performance on a complex road geometry. Unlike the constant curvature of Scenario 1, this scenario features a demanding sequence of varying radius turns, transient maneuvers, and high-speed sections. This benchmark is specifically designed to validate the integrated AOLQI and Stanley architecture's ability to maintain path tracking precision under changing lateral acceleration demands.

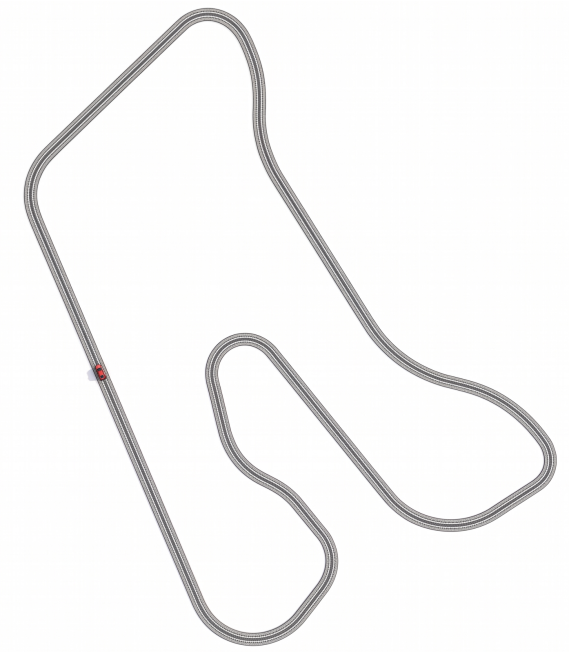

Figure 10. Scenario 2: Hockenheim race track in IPG CarMaker.

The comparative performance of the evaluated control architectures on the complex geometry of the Hockenheim race track is illustrated in Figure 11. As depicted in the lateral deviation analysis in Figure 11a, although all control approaches successfully followed the track, the proposed integrated architecture achieves superior tracking precision. The lateral deviation is remained significantly lower than benchmark controllers throughout the maneuver. This performance increase is attributed to the integration of the Stanley geometric steering law, which facilitates rapid compensation for cross-track errors a critical requirement for rapid transitions of the Hockenheim race track.

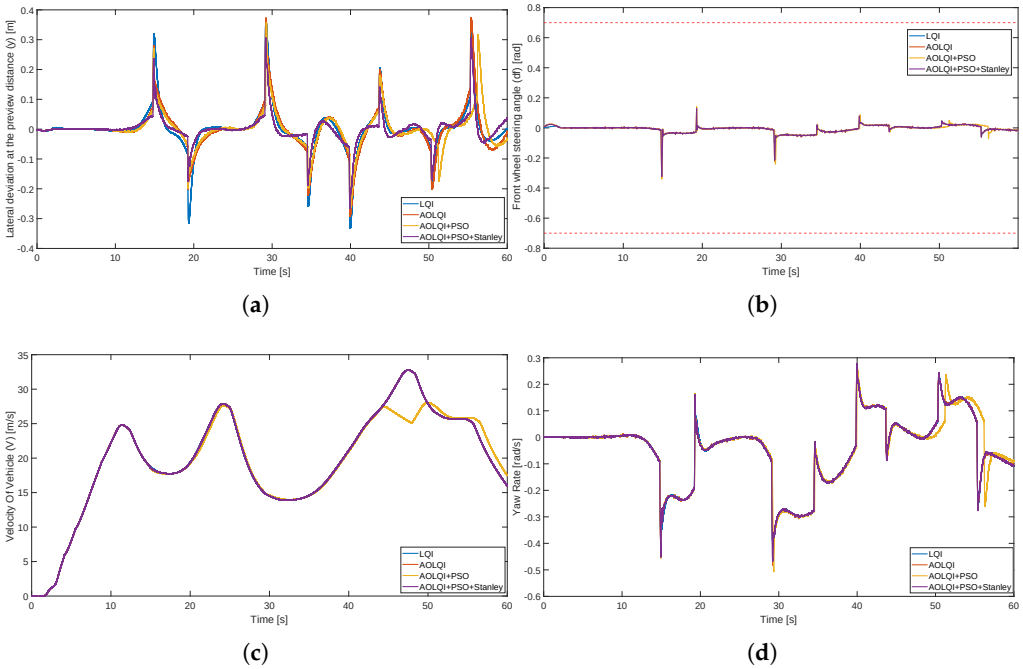

Figure 11. Simulation results for Scenario−2 (Hockenheim race track): (**a**) lateral deviation at the preview distance (e_y) [m], (**b**) front wheel steering angle (δ_f) [rad], (**c**) vehicle velocity (V) [m/s], and (**d**) yaw rate ($\dot{\psi}$) [rad/s].

The front-wheel steering angle (δ_f) profiles, shown in Figure 11b. Using the proposed control approach, the front-wheel steering angle values at the peak points are lower than those of the benchmark controllers in conjunction with Scenario 1.

While most systems followed the target velocity profile, the results in Figure 11c indicate that the AOLQI+PSO control system struggles to attain the maximum expected vehicle speed. This performance gap underscores how uncompensated lateral deviations can degrade overall vehicle dynamic performance. In contrast, the proposed integrated system maintains the desired speed profile with high fidelity, ensuring that lateral control efforts do not compromise longitudinal control performance.

Consistent with the steering and velocity results, the yaw rate response illustrated in Figure 11d shows noticeable delays for the AOLQI+PSO control system. In contrast, the other architectures, particularly the proposed system, exhibit favorable yaw dynamics behavior.

4.5. Scenario 3: ITA Stelvio Pass Road Profile Test

The final evaluation scenario is conducted on the ITA Stelvio Pass road profile defined in the IPG CarMaker environment. Characterized by its iconic tight hairpin turns and continuous elevation changes, this Italian road scenario represents the ultimate benchmark for testing the agility and adaptability of the proposed integrated controller. The high frequency of sharp directional changes requires the AOLQI control approach to rapidly update the control gains while the Stanley control maintains geometric alignment under extreme curvature.

The comparative performance of the investigated control architectures on the extreme mountain road profile of the Stelvio Pass is illustrated in Figure 12.

As demonstrated in the lateral deviation analysis in Figure 13a, the proposed integrated architecture exhibits exceptional efficacy, achieving its highest relative path tracking precision across all evaluated scenarios. In this scenario, the vehicle operates at reduced velocities necessitated by the acute turns, which inherently limits the geometric contribution

of the Stanley control. However, the AOLQI control successfully compensates for this by capturing rapid variations and providing instantaneous road adaptation. Consequently, the lateral deviation is substantially reduced compared to the benchmark controllers.



Figure 12. Scenario 3: ITA Stelvio Pass road profile in IPG CarMaker.

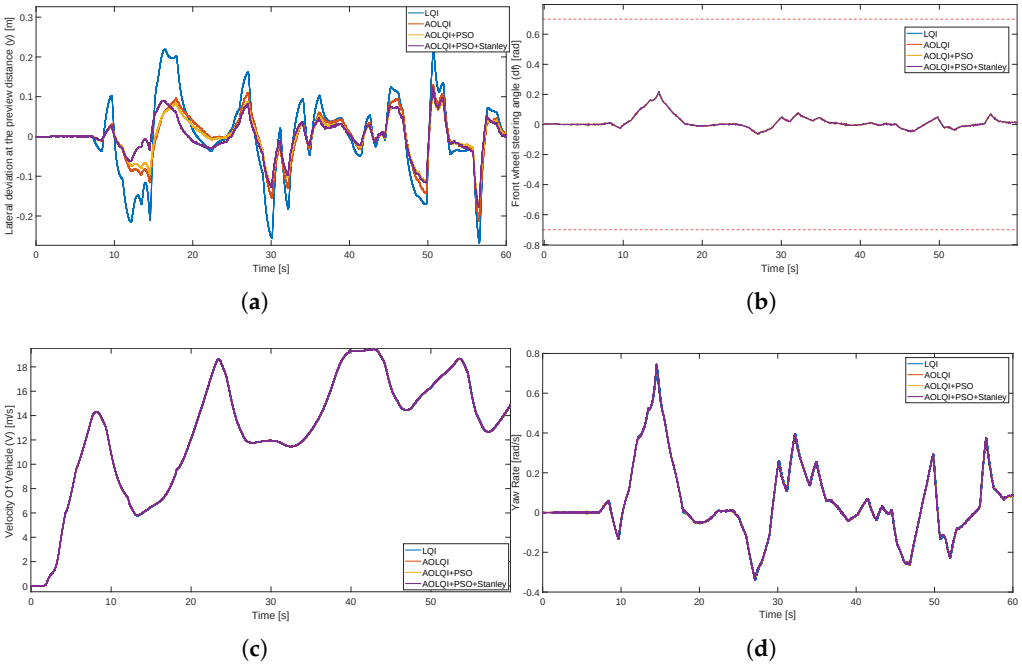

Figure 13. Simulation results for Scenario−3 (ITA Stelvio Pass Road Profile): (**a**) Lateral deviation at the preview distance (e_y) [m], (**b**) Front wheel steering angle (δ_f) [rad], (**c**) Vehicle velocity (V) [m/s], and (**d**) Yaw rate ($\dot{\psi}$) [rad/s].

Regarding the steering control signals (δ_f) depicted in Figure 13b, all control systems maintain high-magnitude steering inputs while maintaining smooth command transitions. The steering commands are remained well within the operational limits of the actuators, following the path's curvature without inducing saturation.

Furthermore, the velocity profiles shown in Figure 13c exhibit significant variability, reflecting the continuous acceleration and braking cycles inherent to navigating mountain passes. All control systems manages these velocity fluctuations effectively. The yaw rate

response illustrated in Figure 13d confirms that all vehicles with different control systems behave within the yaw limits of vehicle stability and occupant comfort.

In autonomous driving applications, geometric controllers such as the Stanley controller are limited in that a position gain (k_y) cannot achieve both low-speed maneuverability and high-speed lateral stability. However, since the path will be known to the autonomous vehicle, gain sets prepared for various scenarios can be selected automatically according to the path. Taking this approach into account, the parameters of the Stanley controller tuned for each scenario to improve path tracking performance across diverse driving conditions. Specifically, the position gain (k_y) is adjusted to accommodate the unique curvature demands and transient complexities inherent to each test scenario. Increasing the gain facilitated more aggressive error correction in high-curvature segments, such as those found in the Stelvio Pass, whereas more conservative values are utilized for high-speed stability in the 100-m radius circular path test and Hockenheim race track. The final scenario-specific tuning configurations for the modified Stanley controller are summarized in Table 6.

Table 6. Scenario-specific tuning parameters for the geometric control layer.

Parameter	Symbol	Scenario 1	Scenario 2	Scenario 3
Position Gain	k_y	2.0	0.5	1.3
Steering Rate Damping	$k_{d,steer}$	0.01	0.01	0.003
Softening Constant	k_{soft}	0.3	0.3	0.3
Yaw Rate Damping Gain	$k_{d,yaw}$	0.1	0.1	0.1

4.6. Performance Evaluation

To provide a quantitative assessment of the proposed control architecture's path tracking precision across the three diverse scenarios, two widely recognized performance indices are utilized: Root Mean Square Error (RMSE) and Integral Square Error (ISE). These metrics evaluate the lateral deviation at the preview distance (e_y) from different perspectives.

The RMSE is employed to measure the average deviation of the vehicle from the reference path. A lower RMSE value indicates higher overall path tracking consistency. It is defined as:

$$RMSE = \sqrt{\frac{1}{N}\sum_{k=1}^{N} e_y(k)^2} \tag{47}$$

where N is the total number of samples over the simulation horizon T and $e_y(k)$ is the lateral deviation at the preview distance for the k-th time step.

The ISE index penalizes larger errors more heavily than smaller ones due to the squaring of the error term. It provides a measure of the total error throughout the maneuver, defined by:

$$ISE = \sum_{k=1}^{N} e_y(k)^2 \Delta t \tag{48}$$

where the sampling interval Δt is 0.001 s.

The quantitative evaluation of the tracking performance, as derived from the RMSE and ISE metrics, is presented in Table 7 to provide a comprehensive comparison of the Stanley, conventional LQI, AOLQI, PSO-optimized AOLQI, and the proposed integrated AOLQI+PSO+Stanley system. Owing to the structural characteristics of the standalone Stanley controller, it exhibits a relatively high transient error during aggressive maneuvers. In contrast, the state-feedback and integral action capabilities of the LQI and its advanced variants significantly mitigate these transient deviations, leading to a substantial performance gap between the standalone geometric and optimal control paradigms. To

rigorously quantify and evaluate these trajectory tracking improvements, the conventional LQI controller is designated as the fundamental baseline for all comparative analyses.

In Scenario-1 (Circular Path), the proposed controller shows a 44.85% reduction in RMSE and a 69.2% improvement in ISE relative to the benchmark LQI control system. These gains are further sustained in Scenario-2 (Hockenheim race track), the proposed control architecture achieves a 24.76% improvement in RMSE and a 43.16% reduction in ISE.

Table 7. Quantitative tracking performance comparison (RMSE and ISE) across all simulation scenarios ($\mu = 1$).

Control Systems	Scenario-1		Scenario-2		Scenario-3	
	RMSE	ISE	RMSE	ISE	RMSE	ISE
Stanley	0.8679	45.7100	1.8197	200.2400	0.7387	32.9250
LQI	0.0214	0.0275	0.0755	0.3422	0.0961	0.5540
AOLQI	0.0135	0.0111	0.0726	0.3208	0.0577	0.2017
AOLQI+PSO	0.0123	0.0092	0.0602	0.2203	0.0473	0.1354
AOLQI+PSO+Stanley	0.0118	0.0085	0.0568	0.1945	0.0471	0.1337

The most significant performance advancements are observed in Scenario-3 (Stelvio Pass), which yielded a 51% improvement in RMSE and a 75.86% reduction in ISE. This represents the highest path tracking success among the tested scenarios and shows the system's exceptional capability in tracking high-curvature segments.

To further evaluate the performance and adaptability of the proposed control architecture, Scenario 1 was additionally executed under varying tire–road friction coefficients ($\mu = 0.8$ and $\mu = 0.5$). The quantitative tracking performance metrics (RMSE and ISE) for all evaluated control systems under these adverse surface conditions are summarized in Table 8. As anticipated, the lateral tracking errors increase for all controllers as the friction coefficient decreases from $\mu = 0.8$ to $\mu = 0.5$ due to the reduced tire force generation capacity. However, the proposed AOLQI+PSO+Stanley integrated control system consistently maintains superior path tracking precision across both friction conditions. Specifically, under the high-friction condition ($\mu = 0.8$), the proposed framework achieves a 30.70% reduction in RMSE and a 50.90% reduction in ISE compared to the baseline LQI controller. Even under the low-friction condition ($\mu = 0.5$), the proposed system outperforms the baseline LQI by 10.82% in RMSE and 19.23% in ISE.

Table 8. Quantitative tracking performance comparison (RMSE and ISE) under varying tire–road friction coefficients ($\mu = 0.8$ and $\mu = 0.5$) for Scenario 1.

Control Systems	Scenario 1 ($\mu = 0.8$)		Scenario 1 ($\mu = 0.5$)	
	RMSE	ISE	RMSE	ISE
Stanley	0.8677	45.6700	0.9036	49.5530
LQI	0.0215	0.0277	0.0573	0.1971
AOLQI	0.0163	0.0161	0.0519	0.1645
AOLQI+PSO	0.0154	0.0144	0.0518	0.1639
AOLQI+PSO+Stanley	0.0149	0.0136	0.0511	0.1592

The significant reduction in both the RMSE and ISE metrics mainly stems from three distinct mechanisms: (i) the integral action embedded within the LQI framework that mathematically eliminates steady-state lateral offsets; (ii) the continuous online update of system dynamics, driven by real-time FFRLS and Kalman–Bucy filter state estimates, which dynamically adapts the controller behaviour; and (iii) the integration of the Stanley geometric controller, which improves path tracking performance.

In addition to path tracking accuracy, the control effort and actuator demand represent crucial performance indices for evaluating the feasibility and physical constraints of the proposed control architecture. To quantify the steering effort across all evaluated controllers, the maximum absolute value of the front wheel steering angle (denoted as peak steering effort, max $|\delta_f|$) was evaluated. Table 9 summarizes the peak steering effort performance across the three benchmark tracks. Furthermore, Table 10 presents the peak steering effort under adverse tire–road friction conditions ($\mu = 0.8$ and $\mu = 0.5$) for the circular path test scenario.

Table 9. Comparison of the peak steering effort (max $|\delta_f|$ in radians) across benchmark driving scenarios.

Control Systems	Scenario 1	Scenario 2	Scenario 3
Stanley	0.0756	0.1700	0.2388
LQI	0.0657	0.0961	0.2118
AOLQI	0.4553	0.3260	0.2198
AOLQI+PSO	0.4658	0.3413	0.2194
AOLQI+PSO+Stanley	0.4251	0.3245	0.2206

Table 10. Comparison of the peak steering effort (max $|\delta_f|$ in radians) under varying tire–road friction coefficients ($\mu = 0.8$ and $\mu = 0.5$) for Scenario 1.

Control Systems	Scenario 1 ($\mu = 0.8$)	Scenario 1 ($\mu = 0.5$)
Stanley	0.0771	0.1136
LQI	0.0787	0.6224
AOLQI	0.6116	0.7000
AOLQI+PSO	0.6173	0.7000
AOLQI+PSO+Stanley	0.5805	0.7000

As it can be seen from Tables 9 and 10, the relatively higher peak steering effort observed in the adaptive schemes conclusively demonstrates that the proposed architecture operates more aggressively and dynamically allocates steering control signal to aggressively suppress and minimize lateral path tracking errors. While standard fixed-gain linear controllers exhibit lower peak steering demands in steady-state circle maneuvers, they suffer from significant tracking degradation, particularly under low-friction regimes. Conversely, the proposed AOLQI+PSO+Stanley framework increases steering authority to compensate for reduced lateral tire forces and sharp track curvatures, even reaching the predefined actuator saturation limit (0.7000 rad) under adverse conditions ($\mu = 0.5$) to ensure tracking safety. Crucially, the integration of PSO weighting optimization and Stanley control action within the proposed framework systematically mitigates excessive overshoot compared to pure AOLQI, achieving an optimal trade-off between aggressive error elimination and physical actuator constraints.

5. Conclusions

This paper presented the development, evaluation and numerical validation of a comprehensive control architecture designed specifically for autonomous vehicle path tracking within a high-fidelity co-simulation environment. An adaptive online LQI control system was integrated with a Stanley geometric control system and tire cornering stiffnesses and vehicle side-slip angle estimations to improve autonomous vehicle path tracking performance. This control framework was structured into three functional layers: the initialization layer for initial controller optimization, the estimation layer for tire cornering stiffness values and the vehicle side-slip angle estimation and the control layer for integrated path tracking control.

The performance of the proposed method was evaluated and compared against benchmark baseline controllers (including the standard Stanley controller and conventional LQI

variants) using high-fidelity MATLAB/Simulink and IPG CarMaker co-simulation scenarios, such as a 100-m constant radius circular path, the high-speed Hockenheim race track, and the high-curvature Stelvio Pass. Simulation results demonstrated that the proposed control approach achieved superior tracking accuracy, reducing lateral deviation in terms of root mean square error (RMSE) and integral square error (ISE).

This study's primary achievements were the offline optimization of the AOLQI using the PSO algorithm, and the successful integration of the Stanley control system to enhance path tracking performance. The efficacy of the proposed control framework was significantly enhanced by adaptation mechanisms. Specifically, a Forgetting Factor Recursive Least Squares (FFRLS) algorithm was utilized for dynamic tire cornering stiffness estimation, combined with a Kalman–Bucy filter for vehicle side-slip estimation.

Future work will focus on experimentally validating the proposed control architecture on an autonomous test vehicle to evaluate real-world trade-offs including hardware execution latency, sensor noise, and actuator dynamics—alongside refining the estimation layer with nonlinear observers such as the Extended Kalman Filter (EKF) and Unscented Kalman Filter (UKF) and benchmarking against optimization-based strategies like Model Predictive Control (MPC).

Author Contributions: Conceptualization, B.S. and M.T.E.; methodology, B.S. and M.T.E.; software, B.S.; validation, B.S. and M.T.E.; formal analysis, B.S.; investigation, B.S.; resources, B.S. and M.T.E.; data curation, B.S.; writing—original draft preparation, B.S. and M.T.E.; writing—review and editing, B.S. and M.T.E.; visualization, B.S. and M.T.E.; supervision, M.T.E.; project administration, M.T.E.; funding acquisition, B.S. and M.T.E. All authors have read and agreed to the published version of the manuscript.

Funding: This research received no external funding.

Data Availability Statement: The original contributions presented in this study are included in the article. Further inquiries regarding the simulation data can be directed to the corresponding author.

Acknowledgments: The authors would like to thank IPG Automotive and Semi-Mobility Technology for providing the IPG CarMaker software (version 14.0) as part of the Solutions for Academics program, which supports PhD dissertations.

Conflicts of Interest: The authors declare no conflicts of interest.

Abbreviations

The following abbreviations are used in this manuscript:

4WIS/4WID/4WIB	Four-wheel independent steering, driving, and braking
AOLQI	Adaptive online linear quadratic integral
CG	Center of gravity
DOF	Degree of freedom
FFRLS	Forgetting factor recursive least squares
GA	Genetic algorithm
ISE	Integral square error
KF	Kalman–Bucy filter
LQI	Linear quadratic integral
LQR	Linear quadratic regulator
LTV	Linear time varying
PID	Proportional derivative integral
PSO	Particle swarm optimization
RMSE	Root mean square error

References

1. Emirler, M.T.; Wang, H.; Aksun Güvenç, B.; Güvenç, L. Automated robust path following control based on calculation of lateral deviation and yaw angle error. In Proceedings of the ASME 2015 Dynamic Systems and Control Conference, Columbus, OH, USA, 28–30 October 2015; p. V003T50A009.
2. Emirler, M.T.; Wang, H.; Aksun Güvenç, B. Socially acceptable collision avoidance system for vulnerable road users. *IFAC-PapersOnLine* **2016**, *49*, 436–441. [CrossRef]
3. Wang, H.; Tota, A.; Aksun Güvenç, B.; Güvenç, L. Real time implementation of socially acceptable collision avoidance of a low speed autonomous shuttle using the elastic band method. *Mechatronics* **2018**, *50*, 341–355. [CrossRef]
4. Wang, H.; Gelbal, S.Y.; Güvenç, L. Multi-objective digital PID controller design in parameter space and its application to automated path following. *IEEE Access* **2021**, *9*, 43339–43350. [CrossRef]
5. Emirler, M.T. Speed dependent gain scheduled LQI based path following control system design for automated vehicles. *Gazi Univ. J. Sci. Part C Des. Technol.* **2019**, *7*, 855–868. (In Turkish)
6. Tajdari, F.; Ramezanian, H.; Paydarfar, S.; Lashgari, A.; Maghrebi, S. Flow metering and lane-changing optimal control with ramp-metering saturation. In *Proceedings of the 2022 CPSSI 4th International Symposium on Real-Time and Embedded Systems and Technologies (RTEST), Tehran, Iran, 30–31 May 2022*; IEEE: New York, NY, USA, 2022; pp. 1–6.
7. Rakhshani, E.; Naveh, I.M.H.; Mehrjerdi, H.; Pan, K. An optimized LQG servo controller design using LQI tracker for VSP-based AC/DC interconnected systems. *Int. J. Electr. Power Energy Syst.* **2021**, *129*, 106752. [CrossRef]
8. Moradi, B.; Moradi, K.; Bauer, P.; Shafiee, Q. Data-Driven Control of DC-DC Boost Converters Interfaced with Constant Power Loads. In *Proceedings of the 2025 IEEE Seventh International Conference on DC Microgrids (ICDCM), Tallinn, Estonia, 4–6 June 2025*; IEEE: New York, NY, USA, 2025; pp. 1–6.
9. Mohan, A.M.; Meskin, N.; Mehrjerdi, H. LQG-based virtual inertial control of islanded microgrid load frequency control and DoS attack vulnerability analysis. *IEEE Access* **2023**, *11*, 42160–42179. [CrossRef]
10. Grube, M.; Wieck, J.C.; Seifried, R. Comparison of modern control methods for soft robots. *Sensors* **2022**, *22*, 9464. [CrossRef]
11. Karthick, S.; Kanthalakshmi, S.; Vinodh Kumar, E.; Joshi Kumar, V.; Ezhil Kumaran, A. Experimental validation of adaptive augmented LQI control for a 2 DoF helicopter. *IETE J. Res.* **2024**, *70*, 584–596. [CrossRef]
12. Saleem, O.; Kazim, M.; Iqbal, J. Robust position control of VTOL UAVs using a linear quadratic rate-varying integral tracker: Design and validation. *Drones* **2025**, *9*, 73. [CrossRef]
13. Ahmdia, A.; Ibrahim, M.; Sarhan, A.; Elsaid, A.E. Comparative Analysis of Optimal Controllers Performance for Unmanned Aerial Vehicles. In *Proceedings of the 2025 15th International Conference on Electrical Engineering (ICEENG), Cairo, Egypt, 12–15 May 2025*; IEEE: New York, NY, USA, 2025; pp. 1–6.
14. Sevim, B.; Emirler, M.T. Design and simulation of linear quadratic integral path following control system based on particle swarm optimisation for autonomous vehicles. In Proceedings of the TOK'2024 25th National Automatic Control Conference, Konya, Türkiye, 12–14 September 2024; pp. 529–535. (In Turkish)
15. Lahmar, O.; Abdou, L.; Ghiloubi, I.B.; Drid, A. Robustness analysis of LQR-PID controller based on PSO and GWO for quadcopter attitude stabilization. *Eng. Proc.* **2025**, *87*, 105. [CrossRef]
16. Wang, Z.; Yao, Y.; Li, Y.; Yang, L.; Zhang, Q. Optimization of Hypersonic Aircraft Fuel Thermal Management System Based on LQI-PSO. In *Proceedings of the 2025 IEEE/ASME International Conference on Advanced Intelligent Mechatronics (AIM), Hangzhou, China, 14–18 July 2025*; IEEE: New York, NY, USA, 2025; pp. 1–6.
17. Dinh, C.T.; Huynh, T.; Kim, Y.B. LQI control system design with GA approach for flying-type firefighting robot using waterpower and weight-shifting mechanism. *Appl. Sci.* **2022**, *12*, 9334. [CrossRef]
18. Cai, Y.; Chen, Q.; Shu, Q.; Liu, S.; Yu, X. Joint estimation of tire cornering stiffness and vehicle operating state for distributed drive electric vehicles. *Asian J. Control* **2025**, *early view*. [CrossRef]
19. Qin, Z.; Wang, J.; Liu, P.; Han, Y.; Guo, J.; Hong, H.; Chang, Y.; Shen, S. Real time tire stiffness estimation using enhanced GDM and RLS for autonomous vehicles. *Sci. Rep.* **2025**, *15*, 31863. [CrossRef]
20. Hoffmann, G.M.; Tomlin, C.J.; Montemerlo, M.; Thrun, S. Autonomous automobile trajectory tracking for off-road driving: Controller design, experimental validation and racing. In *Proceedings of the 2007 American Control Conference, New York, NY, USA, 9–13 July 2007*; IEEE: New York, NY, USA, 2007; pp. 2296–2301.
21. Cao, H.; Zoldy, M. Implementing B-spline path planning method based on roundabout geometry elements. *IEEE Access* **2022**, *10*, 81434–81446. [CrossRef]
22. Jeong, Y.; Yim, S. Path tracking control with four-wheel independent steering, driving and braking systems for autonomous electric vehicles. *IEEE Access* **2022**, *10*, 74733–74746. [CrossRef]
23. Hocaoglu, Y.; Akcal, A.; Tuncel, A.; Celik, B. A stanley controller design for enhancing vehicle lane keeping and departure performance using active rear wheel steering. In *Proceedings of the 2023 European Control Conference (ECC), Bucharest, Romania, 13–16 June 2023*; IEEE: New York, NY, USA, 2023; pp. 1–6.

24. Seiffer, A.; Frey, M.; Gauterin, F. Pragmatic and effective enhancements for Stanley Path-tracking controller by considering system delay. *Vehicles* **2023**, *5*, 615–636. [CrossRef]
25. Al-Jumaili, M.H.; Özok, Y.E. New control model for autonomous vehicles using integration of Model Predictive and Stanley based controllers. *Sci. Rep.* **2024**, *14*, 19872. [CrossRef]
26. Jnadi, A.; Almaghout, K.; Pronin, A. Performance evaluation of PID, stanley, and hybrid (PID with stanley) control algorithms on bitum line-follower road coaster. In *Proceedings of the 2024 International Ural Conference on Electrical Power Engineering (UralCon), Magnitogorsk, Russia, 27–29 September 2024*; IEEE: New York, NY, USA, 2024; pp. 770–774.
27. Xiao, J.; Li, S.; Wang, N.; Sheng, Q.; Wang, T.; Li, H.; Zhang, M. An Adaptive Double Closed-Loop Path Tracking Control Method for High-Precision Autonomous Navigation of Agricultural Machinery. *J. Field Robot.* **2025**, *43*, 2407–2427. [CrossRef]
28. Emirler, M.T. Path Following Control System Design and Analysis of Autonomous Vehicles. In *Autonomous Vehicles and Systems*; River Publishers: Gistrup, Denmark, 2024; pp. 335–360.
29. Sevim, B.; Emirler, M.T. Autonomous vehicle path following system design using a combined control approach. *Proc. Inst. Mech. Eng. Part D J. Automob. Eng.* **2026**, *240* , 6824–6838. [CrossRef]
30. Saleem, O.; Iqbal, J.; Afzal, M.S. A robust variable-structure LQI controller for under-actuated systems via flexible online adaptation of performance-index weights. *PLoS ONE* **2023**, *18*, e0283079. [CrossRef]
31. The MathWorks, Inc. Kalman Filter. Online Documentation. 2026. Available online: https://www.mathworks.com/help/control/ref/kalmanfilter.html (accessed on 8 July 2026).
32. Ioannou, P.A.; Sun, J. *Robust Adaptive Control*; Dover Publications, Inc.: Mineola, NY, USA, 2012.
33. Simon, D. *Optimal State Estimation: Kalman, H-Infinity, and Nonlinear Approaches*; John Wiley & Sons: Hoboken, NJ, USA, 2006.
34. Anderson, B.D.O.; Moore, J.B. *Optimal Control: Linear Quadratic Methods*; Dover Publications, Inc.: Mineola, NY, USA, 2007.
35. Khalil, H.K. *Nonlinear Systems*, 3rd ed.; Prentice Hall: Upper Saddle River, NJ, USA, 2002.

Disclaimer/Publisher's Note: The statements, opinions and data contained in all publications are solely those of the individual author(s) and contributor(s) and not of MDPI and/or the editor(s). MDPI and/or the editor(s) disclaim responsibility for any injury to people or property resulting from any ideas, methods, instructions or products referred to in the content.